# Experimental Study of Temperature and CH Radical Location in Partially Premixed CH$_4$/Air Coflow Flames

LINDA G. BLEVINS*, MICHAEL W. RENFRO, KENT H. LYLE[†],
NORMAND M. LAURENDEAU, AND JAY P. GORE

*School of Mechanical Engineering, Purdue University, West Lafayette, IN 47907-1288 USA*

As part of an ongoing investigation of an exhaust NO$_x$ emission index minimum measured for partially premixed flames, radial temperature profiles and CH radical locations were measured in atmospheric-pressure, partially premixed, coflow, methane/air flames with fuel-side equivalence ratios of 1.6, 2.0, and 3.5, at three axial heights above the burner. The work was undertaken because of the importance of temperature and CH radical behavior in NO formation chemistry. Thin-filament pyrometry was found to be more appropriate than thermocouple thermometry for temperature measurements in partially premixed flames. Results demonstrated that the 1.6-equivalence-ratio flame exhibited classical double-flame structure, the 2.0-equivalence-ratio flame was a merged flame, and the 3.5-equivalence-ratio flame exhibited diffusion-flame structure. Signals from CH* chemiluminescence and CH laser-induced fluorescence provide evidence that, for the present measurement locations, double flames exhibit single CH peaks which can be associated with their premixed component flames. Double CH radical peaks, which were predicted to occur in low-strain-rate flames, were not found for the limited number of flame conditions and locations studied. In the near-burner region, the premixed and nonpremixed component flames of the $\Phi_B = 1.6$ double flame diverge radially with increasing downstream distance and merge together for larger values of $\Phi_B$. © 1999 by The Combustion Institute

## INTRODUCTION

Partial premixing exists in a flame when a portion of the combustion air mixes with the fuel to form fuel-rich regions surrounded by air. At relatively high levels of partial premixing, a "double flame" is formed. The double flame consists of a rich premixed flame and a nonpremixed flame formed at the interface between the rich combustion products and the surrounding air. Partial premixing occurs in a variety of practical situations, including lifted flames in furnaces, gas-turbine combustor flames, confined radiant heating tube flames, and domestic appliance flames.

Past studies of partial premixing addressed laminar counterflow [e.g., 1–15], laminar jet [e.g., 16–21], unsteady co-annular [e.g., 22, 23], turbulent jet [e.g., 24–33], and practical-burner [e.g, 34, 35] flames. Gore and Zhan measured the exhaust NO$_x$ emission index (EINO$_x$, g NO$_x$ per kg fuel consumed) from laminar, coflow,

methane/air flames with constant global equivalence ratio and found that EINO$_x$ decreased to a minimum value and then increased as air was incrementally added to the fuel jet [16]. Similar EINO$_x$ behavior was found for laminar, coflow, partially premixed ethane/air flames [18], for turbulent, coflow, partially premixed natural gas/air flames [32–33], and for laminar, counterflow, partially premixed CH$_4$/air flames [8]. Collectively, these studies suggest that an optimum operating condition for a partially premixed flame in a practical combustor can be selected which minimizes the amount of NO$_x$ emitted. The present experimental study is part of an ongoing investigation of the exhaust EINO$_x$ minimum measured from partially premixed flames and reported in Refs. 8, 16, 18, and 32–33. The overall goals of the ongoing effort are (1) to contribute to the present understanding of NO$_x$ formation and destruction in flames, and (2) to enable the future design of clean-burning practical combustors which take advantage of the partially premixed EINO$_x$ behavior.

In recent computational studies of low-strain-rate counterflow methane/air double flames, a flame structure characterized by two CH radical concentration peaks was found [10, 15]. One peak occurred at the location of the rich CH$_4$/air premixed flame and the other at the fuel-side

---

* Corresponding author. Present address: Building and Fire Research Laboratory, National Institute of Standards and Technology, Gaithersburg, MD. E-mail: linda.blevins@nist.gov
[†] Present address: Precision Combustion, Inc., New Haven, CT.

edge of the nonpremixed flame formed between the rich products and air. Other hydrocarbon intermediates (e.g., $CH_2$, $CH_3$) also exhibited double concentration peaks. Broad NO destruction regions, caused by $CH_i$ + NO reactions ($i$ = 1, 2, or 3) and by HCCO + NO reactions, existed between the hydrocarbon concentration peaks [15]. Hence, hydrocarbon/NO interactions can occur in the region between the two component flames of a low-strain counterflow double flame, and the existence of double CH peaks indicates that these interactions take place. It is possible that a flame with a broad range of strain rates, such as a coflow partially premixed jet flame, will exhibit regions for which NO formation is similar to that computed for the low-strain-rate flames of Ref. 15. Motivated by this possibility, the primary goal of the present study was to measure temperatures and identify CH radical radial locations in a set of partially premixed, coflow Bunsen-type flames for which the $EINO_x$ minimum has been previously measured [16]. To the authors' knowledge, CH radical measurements in partially premixed coflow jet flames have not been previously published. Nguyen et al. reported local measurements of major species concentrations, temperature, and OH and NO concentrations for partially premixed $CH_4$/air flames with fuel-side equivalence ratios of 1.38, 1.52, and 1.70, but CH radicals were not measured [19].

For the present investigation, burner operating conditions and measurement locations were selected to match some of those used by Gore and Zhan [16]. While these authors measured major species concentrations, flame heights, radiative heat loss, and $EINO_x$, the present work provides radial temperature profiles, axial velocity profiles, and CH radical radial locations. It was necessary to use thin-filament pyrometry (TFP) for measuring temperature because thermocouples exhibited large errors caused by surface ignition in the central fuel/air mixture of these flames [36]. The TFP technique described in this paper features a unique thermocouple-based calibration (performed away from the central unburned-mixture region) as well as corrections for radiative heat loss computed using actual measured velocities. The CH radical locations were determined using chemiluminescence detection and laser-induced fluores-

cence (LIF). The objectives of this study were (1) to implement a calibrated TFP measurement technique appropriate for use in partially premixed Bunsen flames, (2) to examine the structure of partially premixed, coflow $CH_4$/air flames while adding temperature, axial velocity, and CH radical location information to an existing database, and (3) to determine if temperature profiles and CH radical locations at three selected heights within three selected partially premixed flames provide insight into a previously measured exhaust $EINO_x$ minimum for these flames.

## EXPERIMENTS[1]

Experiments were performed in a modified Bunsen burner which allows control of the fuel-stream equivalence ratio. This laminar burner, depicted in Ref. 16, consists of a 15-mm diameter central tube that carries methane premixed with air surrounded by a 100-mm diameter annulus that carries pure coflow air. Flow straightening beads and honeycomb are present in the coflow air stream. Air from a shop compressor was used with commercial grade methane. All rates of flow were measured using rotameters calibrated with a dry-gas meter.

Operating conditions were varied by keeping the rate of fuel flow equal to 42 mg/s (2.1 kW based on lower heating value) and changing the central tube air flow rate to achieve inner tube equivalence ratios ($\Phi_B$) of 1.6, 2.0, and 3.5. The coflowing air was metered so that the global equivalence ratio ($\Phi_{global}$) remained equal to 0.5. A chart of the operating conditions used in the present study and their $NO_x$ emission indices, taken from Ref. 16, is given in Table 1.

Although Ref. 16 contained data from a range of fuel-side equivalence ratios between 1.4 and ∞, only three of these operating conditions were studied in the present work. These three were chosen because $EINO_x$ decreases

---

[1] In order to adequately describe experimental procedures, it is occasionally necessary to identify commercial products by manufacturer's name or label. In no instance does such identification imply endorsement by the National Institute of Standards and Technology, nor does it imply that the particular products or equipment are necessarily the best available for that purpose.

**TABLE 1**

Operating Conditions for Laminar, Partially Premixed Burner [16]

| $\Phi_B$ | Central Air Flow (mg/s) | Central Fuel Flow (mg/s) | Annular Air Flow (mg/s) | EINO$_x$ (g/kg fuel) |
|---|---|---|---|---|
| 1.6 | 450 | 42 | 990 | 2.97 ± 0.30 |
| 2.0 | 360 | 42 | 1080 | 2.29 ± 0.23 |
| 3.5 | 205 | 42 | 1235 | 2.55 ± 0.25 |

between $\Phi_B$ = 1.6 and $\Phi_B$ = 2.0, then increases again between $\Phi_B$ = 2.0 and $\Phi_B$ = 3.5, and any interesting temperature and/or CH radical location trend that might contribute to the EINO$_x$ minimum was expected to be observed for these conditions. Visible flame heights measured with a video camera were 240 mm, 300 mm, and 320 mm, for the $\Phi_B$ = 1.6, 2.0, and 3.5 flames, respectively [37]. All data were collected at axial distances of 20 mm, 40 mm, and 60 mm above the burner. Each of these heights is less than the visible Bunsen-cone tip height for the three conditions studied.

**Temperature**

TFP was used in the present work to measure temperature profiles. The technique was developed by Vilimpoc et al. [38–40], and has been applied in several flame systems [36, 41–45]. The technique involves extending a thin (10–20 $\mu$m) silicon carbide (SiC) fiber with weighted free ends across the radial centerline of the flame and inferring gas temperature from the fiber's measured graybody emission. TFP exhibits rapid time response, excellent spatial resolution, and good signal-to-noise ratio [38].

TFP was selected because thermocouple measurements yielded unrealistically high temperatures in the central unburned region of the flames. This is demonstrated in Fig. 1, which depicts a temperature profile measured with a Pt/Pt13%Rh 0.076-mm wire diameter thermocouple (open squares) and the same profile measured using TFP (closed circles). The profile was measured in a $\Phi_B$ = 2.0 flame at a height of 60 mm above the burner [36]. Both measurement methods were corrected for radiation loss. There is a discrepancy between the results obtained with the two techniques in the
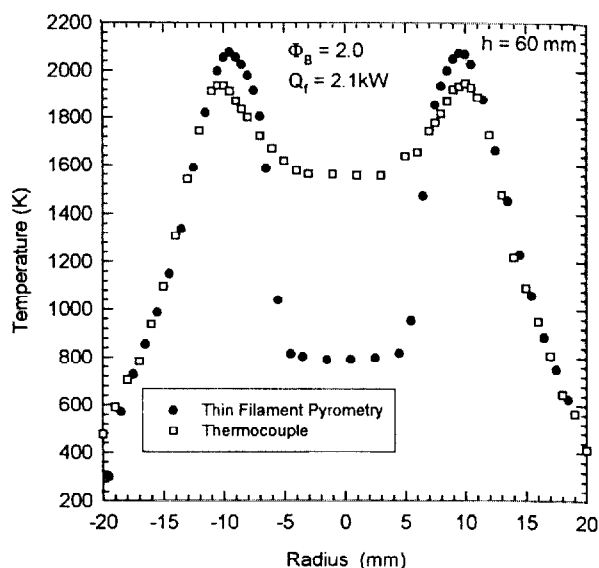


Fig. 1. Thermocouple temperature profile compared with filament temperature profile for $\Phi_B$ = 2.0 flame at a height of 60 mm above the burner surface.

central unburned region of the jet. The thermocouple measurements indicate temperatures of about 1600 K, whereas the TFP measurements indicate temperatures around 800 K. The thermocouple-determined temperatures are unrealistically high in this region because of local ignition caused by heat conducted along the thermocouple leads from the high-temperature flame zone. The TFP technique avoids this problem because the fiber has low thermal conductivity and its surface does not catalyze combustion reactions as readily as that of a thermocouple.

Because calibrated TFP is still a relatively new technique, a few paragraphs are devoted here to describing its current implementation. Further details about the present formulation are available in Refs. 36 and 46. The TFP optical arrangement is shown in Fig. 2. A liquid-nitrogen cooled indium antimonide (InSb) detector, sensitive to radiation between 1.1 $\mu$m and 5.6 $\mu$m, was used with infrared-transmitting calcium fluoride (CaF$_2$) lenses. An adjustable aperture near the flame was used to block flame radiation, and an aperture (slit) near the detector was adjusted to a width of less than 0.1 mm to control the detector peak output signal. The chopper was operated at 300 Hz. The detector output signal was bandpass filtered, conditioned with the 1-second post-filter of a lock-in ampli-
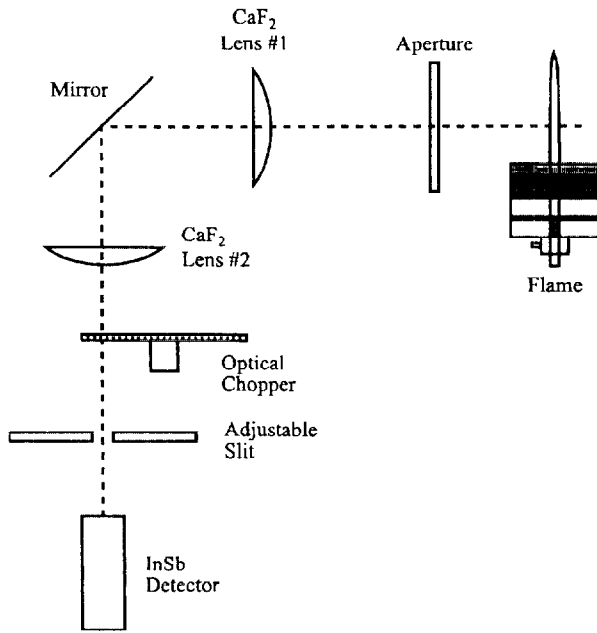
Fig. 2. Schematic of TFP experimental arrangement.

fier, and subsequently sampled at 2 Hz for 5 seconds using a laboratory computer. The long averaging times were possible because the present flames were generally laminar and steady.

The 20-cm-long pieces of fiber (Dow Corning Nicalon SiC, Grade CG, Size PVA, Denier 1800, 15-$\mu$m diameter) were supported as shown schematically in Fig. 3. The fiber was aligned horizontally using a helium–neon (He-Ne) laser with a cylindrical lens. The fiber was aligned along the radial centerline of the flame by ensuring that the distance between temperature peaks in a calibration flame ($\Phi_B$ = 1.6, 20 mm height) was equal to the thermocouple-determined differential distance of 18 mm. Axial variations in fiber diameter, which are a concern when the entire fiber is viewed simultaneously using either array cameras or rapidly scanning mirrors [45], were not important in the present study because a single (constant diameter) point on the fiber was viewed and the flame was traversed across this point.

Since the detector output is directly proportional to the emitted radiation and not to the temperature, conversion of voltage to temperature requires a nonlinear calibration. The present calibration procedure relies on a thermocouple measurement made at a location on the coflow air side of the flame where local

ignition cannot occur. The gas temperature at this specific location is 1000 K, chosen because radiation losses for both the fiber and the thermocouple are small at this temperature. The calibration medium was a 2.1 kW, $\Phi_B$ = 1.6 flame with $\Phi_{global}$ = 0.5. Calibrations were performed at a height of 20 mm above the burner. A primary calibration was performed once using a calibration fiber and a thermocouple measurement. Thereafter, secondary calibrations were performed by relating the signals from each measurement fiber to those of the calibration fiber. The calibration procedure is described in the next few paragraphs.

First, a calibration curve with 1000 K as a reference was produced by numerically integrating the equation

$$A_T = \frac{V_T}{V_{1000K}}$$

$$= \frac{\displaystyle\int_{\lambda_1}^{\lambda_2} \frac{\epsilon C_1}{\lambda^5[\exp(C_2/\lambda T) - 1]} R_{detector}(\lambda)\tau_{optics}(\lambda)\, d\lambda}{\displaystyle\int_{\lambda_1}^{\lambda_2} \frac{\epsilon C_1}{\lambda^5[\exp(C_2/\lambda * 1000K) - 1]} R_{detector}(\lambda)\tau_{optics}(\lambda)\, d\lambda}.$$

(1)

Here, $A_T$ is the signal ratio. The numerator of $A_T$ is the integral with respect to wavelength ($\lambda$) of the filament graybody emission convoluted with the detector response curve ($R_{detector}$) and the optics transmission curve ($\tau_{optics}$). The denominator is the same integral evaluated at 1000 K. In this equation, $C_1$ and $C_2$ are the blackbody curve constants ($C_1$ = 3.742 × $10^8$ W · $\mu$m$^4$/m$^2$; $C_2$ = 1.439 × $10^4$ $\mu$m · K [47]), $V_T$ is the voltage from the fiber emission at temperature $T$, and $V_{1000K}$ is the voltage from the fiber emission at a temperature of 1000 K. The lower and upper limits of integration are $\lambda_1$ = 1.1 $\mu$m and $\lambda_2$ = 5.6 $\mu$m, the limits of the usable range of the detector. The SiC fiber radiates as a graybody with constant emissivity. In the past, $\epsilon$ = 0.88 [38] and $\epsilon$ = 0.92 [44] have been used; in the present work, $\epsilon$ = 0.88 was used following Vilimpoc et al. [38]. The CaF$_2$ optics exhibit a constant transmittance ($\tau_{optics}$ = 0.92) throughout the wavelength range used here [48]. The
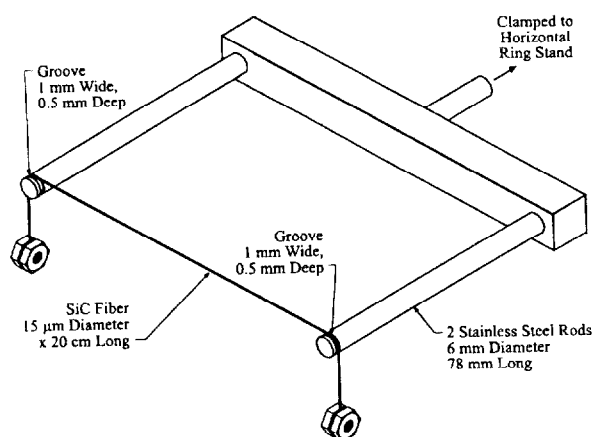
Fig. 3. Schematic of filament holder.

ratio, $A_T = V_T/V_{1000K}$, was computed as a function of temperature and graphed as a calibration curve shown in Fig. 4.

The primary calibration was performed by inserting the calibration fiber into the calibration flame and locating the peak temperature by traversing the burner. Since the temperature at this location was known to be about 2000 K, the system was aligned and the detector gain adjusted until the peak detector voltage was in the range of 5 to 7 V. Next, the radial location corresponding to a temperature of about 1000 K was located by traversing the burner until the filament emission voltage was $V_{1000K} = V_{2000 K}/A_{2000K}$, calculated *a priori* using the value of $A_{2000K}$ from the calibration curve. Next, a 0.076-mm-wire-diam-
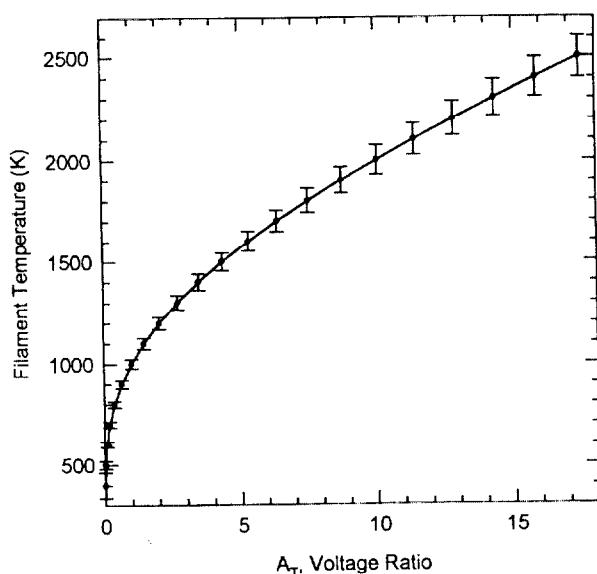


Fig. 4. Temperature calibration chart with error bars.

eter Pt/Pt13%Rh thermocouple was moved along the filament until the detector signal indicated that the filament emission was partially blocked by the thermocouple bead. The primary calibration filament was then broken (removed) to keep it from interfering with the thermocouple measurement. The actual temperature at this location was taken to be equal to that indicated by the thermocouple. Using this known gas temperature/filament voltage pair, the peak temperature in the calibration flame was determined using the calibration curve. The known peak temperature and its known location in the calibration flame were then used to perform a secondary calibration for each measurement fiber.

Details of the TFP uncertainty analysis are given in Ref. 46. The primary component of uncertainty in a TFP measurement arises from the point used for calibration ($V_{1000K}$), which falls on a very steep portion of the radial temperature profile in the calibration flame. Hence, a small uncertainty in the radial location of the calibration thermocouple results in a large uncertainty in the temperature determined by the technique. The slope of the temperature profile in the calibration flame was used along with the estimated uncertainty in the radial location of the calibration thermocouple to determine the uncertainty in $V_{1000K}$. (This is a Type B method as defined in Refs. 49 and 50.) The uncertainty in $V_{1000K}$ was combined with the least-count voltage uncertainty using the root-sum-of-squares method to yield the uncertainty in the calibration voltage ratio, $A_T$. The calibration curve was then perturbed and the resulting combined standard uncertainty in temperature, $t_c$ (estimated standard deviation), was deduced. The unknown value of the temperature is believed to lie in the interval $T \pm t_c$ with a level of confidence of approximately 68%. The uncertainty is as high as 90 K for temperatures of 2200 K, and is depicted using error bars in Fig. 4. The minimum measurable temperature with the InSb detector is 500 K [46], which is in agreement with the lower limit reported by Bedat et al. [44].

For all measurements in the calibration flame and in the other flames, radial scans of the background radiation from flame gases were taken without a filament in place. The flame

emission voltages were subtracted from the voltages resulting from the flame and filament combined. Typical flame emission voltages were about 5–7% of the peak filament emission signal for each measurement.

Temperatures measured using TFP must be corrected for radiation losses to the surroundings. In the present study, the correction was performed using a correlation for a cylinder in forced, low-Reynolds-number crossflow [51, 52],

$$Nu = 0.43 + 0.48Re^{1/2} \qquad (2)$$

In this equation, Nu is the Nusselt number defined as $Nu = hd_f/k_g$, where $h$ is the convective heat transfer coefficient between the flowing gas and the fiber $(W/m^2 \cdot K)$, $d_f$ is the diameter of the fiber $(15 \times 10^{-6}$ m), and $k_g$ is the gas thermal conductivity $(W/m \cdot K)$. The Reynolds number, Re, is defined as $Re = Ud_f/\nu_g$, where $U$ is the crossflow velocity (m/s) and $\nu_g$ is the gas kinematic viscosity $(m^2/s)$. Gas properties $(\nu_g$ and $k_g)$, taken from Ref. 47, were evaluated for air at the film temperature using an iterative procedure. The use of air properties is expected to be adequate because air (consisting primarily of $N_2$) is present throughout partially premixed flames. The crossflow axial velocity was measured using laser Doppler velocimetry (LDV) [32]. Equation 2 was estimated to be correct within 10% for Reynolds numbers as low as 0.1 by Hsu [52]. The present study yielded Reynolds numbers ranging from 0.01 to 1.5, corresponding to Nusselt numbers between 0.5 and 1.0. The radiation correction resulted in temperature corrections as high as 200 K at peak filament temperatures.

## Axial Velocity

The dual-beam, single-channel LDV system, described elsewhere [32, 53], consisted of an argon-ion laser, a beam splitter, a frequency shifter, and a focusing lens. The receiving optics were oriented perpendicularly to the sending optics, and a counter-type burst processor was used. Two fluidized bed seeders were used, one for the center tube premixing air and one for the coflow air. Corrections for thermophoretic effects were not made because the present axial

| | |
|---|---|
| Argon-ion laser wavelength | 514.5 nm |
| Laser beam $(e^{-2})$ diameter | 1.3 mm |
| Focusing lens focal length | 604 mm |
| Beam intersection half-angle | 1.2° |
| Fringe spacing | 6.2 $\mu$m |
| Number of fringes | 48 |
| Probe volume dimensions | 0.3 mm × 0.3 mm × 7.4 mm |
| Collection lens focal length | 604 mm |
| PMT pinhole aperture | 0.2 mm |
| Measuring volume dimensions | 0.3 mm × 0.3 mm × 0.6 mm |
| Frequency shift | 1 MHz |
| Nominal $Al_2O_3$ seed particle size | 0.5 $\mu$m |

velocities are normal to the direction of the most severe thermophoretic forces. An analysis detailed in Ref. 53 revealed that measured velocities were accurate to within ±1%. Important LDV parameters are shown in Table 2 [53].

## CH Radical Location

The radial location of the CH radical was determined using CH* chemiluminescence and laser-induced fluorescence (LIF). Qualitative measurements of the spectral intensity of chemiluminescence emission from CH* $(A^2\Delta$-$X^2\Pi$ transition) at 432 nm were made using an optical arrangement consisting of a 15-mm-long, 8-mm-diameter collimating probe, a 1/8 m monochromator, and an R268 end-on photomultiplier tube (PMT) [46]. A schematic of the CH* arrangement is shown in Fig. 5. The collimating probe was positioned with its receiving end at the outer edge of the visible flame. The monochromator grating had a 350-nm blaze wavelength, 1200 lines/mm, and a reciprocal dispersion of 6.6 nm/mm. The monochromator entrance and exit slits were both set to 0.4 mm to yield a full width at half maximum (FWHM) bandwidth of 3 nm, as measured using a He-Ne laser. The PMT chemiluminescence output signal was low-pass filtered at 50 Hz before being sampled at 100 Hz and computer-averaged for 30 seconds.

For the CH* measurements, the collimating probe was placed in the coflow with its inlet about 10 mm from the burner centerline. This
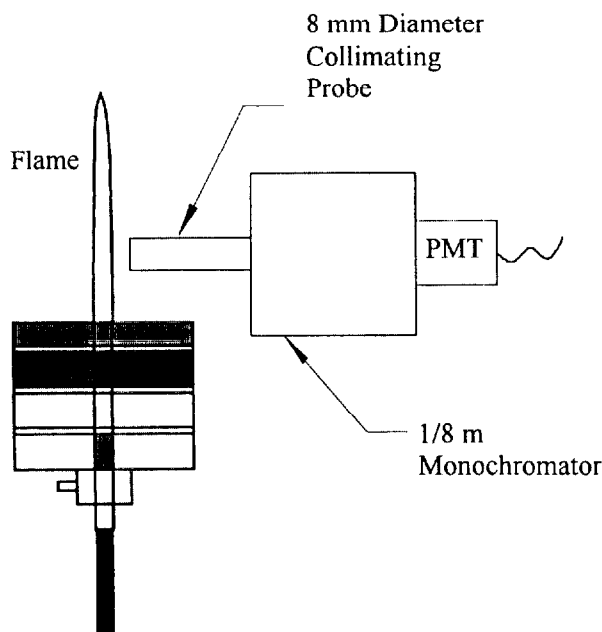
8 mm Diameter
Collimating
Probe

Flame

PMT

1/8 m
Monochromator

Fig. 5. Schematic of arrangement used to detect CH* chemiluminescence.



Fig. 6. Schematic of laser arrangement for CH LIF. P = Polarization Rotator, C = Chopper, R = Radiometer, M = Monochromator.

allowed the probe to be positioned as close as possible to the flame without being placed directly into the flame. The burner was then translated along the axis perpendicular to the collimating probe, and measurements were made at locations which were spaced 0.3 mm to 1 mm apart along this axis. This procedure resulted in large-view-angle measurements. Because the flame was translated and the probe was stationary, the actual view angle varied for each flame location measured. Deconvolution of the resulting broad, line-of-sight CH* profiles yielded unrealistically broad local radial centerline CH* profiles. To obtain spatially resolved information, LIF was used as a second way to identify the locations of CH radical peaks.

Reviews of LIF studies and techniques are available [54, 55]. While it is challenging to determine absolute quantitative CH concentrations using LIF in atmospheric-pressure flames, the aim of this work was to identify only the radial *locations* of CH radical concentration peaks. Hence, CH LIF signals are reported in arbitrary units and are not meant to represent quantitative CH radical concentrations. The *location* of a peak in the LIF signal should be indicative of the *location* of a peak in the CH concentration profile, as long as there is enough laser-excited CH to fluoresce while experienc-
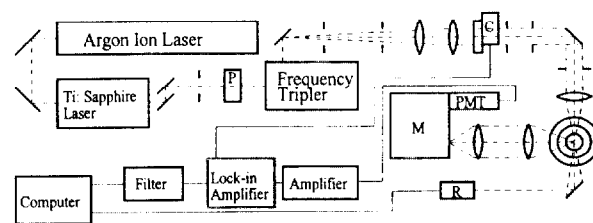
ing collisional quenching. The standard uncertainty (i.e., estimated standard deviation) in the radial LIF-determined CH location is 0.1 mm based on the least count of the translation stage movements.

The details of the LIF technique used in the present work were recently published by Renfro et al. [56, 57]. A schematic of the experimental apparatus is shown in Fig. 6. The Ti:Sapphire mode-locked laser is pumped by a multimode argon-ion laser and delivers a series of mode-locked pulses of 1.5 picosecond FWHM at a repetition rate of 80 MHz. The laser output is frequency doubled, and the spectral width of the beam after doubling is estimated to be 10 cm$^{-1}$ (0.2 nm). The wavelength (430.6 nm) and the spectral width of the laser exiting the doubling crystal permit simultaneous excitation of about 10 Q-branch transitions within the (0,0) band of the A$^2$-X$^2$ system of CH. Spectrally narrower pulses (about 1 cm$^{-1}$) that permit excitation of a single rovibronic line are attainable with the current laser system but with significantly reduced laser power. This alternative strategy was used to excite the temperature-insensitive Q1(1) line (Q1c and Q2c) of CH in a simple nonpremixed methane jet flame and was found to yield the same results as the broadband excitation scheme but with a lower signal-to-noise ratio [57].

Fluorescence emission was collected in a direction perpendicular to the laser beam axis and focused onto the entrance slit of a 1/4 m monochromator. Rayleigh scattering interference was minimized by horizontal polarization of the laser beam. The width of the exit slit of the monochromator was 1 mm, resulting in the detection of fluorescence in a 4-nm region centered about 430 nm. Selected spectral scans performed at the location of peak LIF signal

revealed spectrally narrow features, indicating the absence of fluorescence interference from polyaromatic hydrocarbons (PAH). The probe volume (as defined by the entrance slit of the monochromator and the beam diameter) in the flame was 100 $\mu$m high, 100 $\mu$m wide, and 60 $\mu$m deep; the resulting average laser irradiance was 4.4 × $10^6$ mW/cm². A lock-in amplifier was used to sample the Hamamatsu HS5321 PMT signal, which was then normalized by the independently measured laser power. Rayleigh scattering contributions were determined from a curve fit (of the form $C_1 + C_2/T$) through a point in the unburned fuel/air mixture and a point in the coflow air stream, selected because CH was known to be absent at both points. The curve fit was used along with the TFP-measured temperatures to calculate Rayleigh scattering corrections which were subtracted from the measured signals.

## RESULTS AND DISCUSSION

Figure 7 depicts representative radial profiles of TFP-determined temperature $(T)$ and LDV-determined axial velocity $(U)$ measured at heights $(h)$ of 20 mm, 40 mm, and 60 mm along radial centerlines for the $\Phi_B = 1.6$ flame. For each height, along a radius, the temperature is low near the center of the jet, rises with a steep slope to an inner characteristic temperature, rises approximately linearly with a moderate slope to the peak temperature, and then decreases with a steep slope toward the temperature of the coflow air (300 K). The inner characteristic temperature indicates the approximate location of the rich premixed $CH_4$/air flame, while the outer peak temperature identifies the location of the nonpremixed $CO/H_2$/air flame established at the interface of the products of rich combustion and the coflowing air stream. The temperature-profile shapes are similar to those measured and computed in laminar double flames previously [1–3, 8–12, 14, 19]. The peak flame temperatures are 2260 ± 87 K at heights of 20 mm, 40 mm, and 60 mm above the burner. The adiabatic flame temperature for stoichiometric methane in air (2230 K) falls within this uncertainty interval.

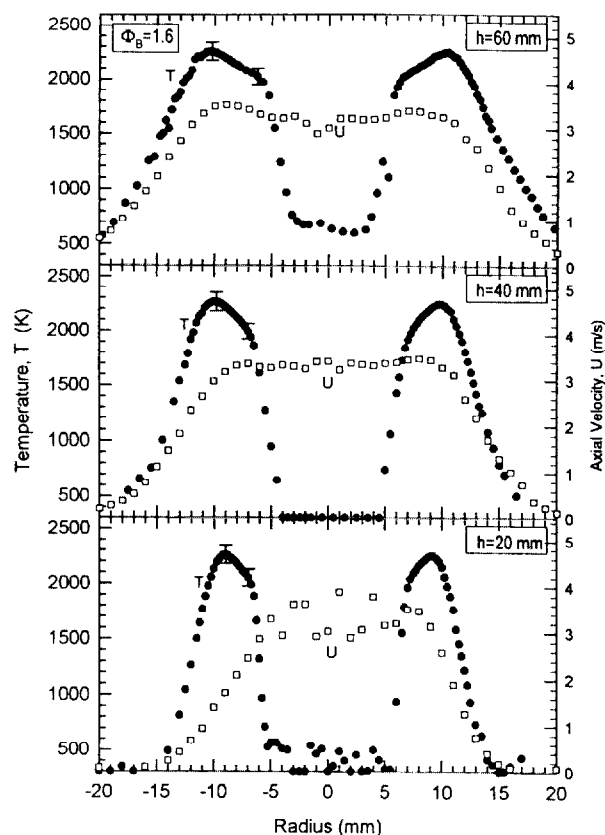At heights of 20 mm and 40 mm above the



Fig. 7. Temperature (T) and axial velocity (U) for positions 20 mm, 40 mm, and 60 mm above the burner in the $\Phi_B = 1.6$ flame.

burner, the temperatures in the center of the jet are less than the minimum detectable temperature of 500 K. It is reasonable that the temperatures at these locations are lower than 500 K because the jet consists of an unburned rich mixture of methane and air in its center. At 60 mm, the temperature in the inner unburned mixture is about 600 K.

Measured axial velocities for the $\Phi_B = 1.6$ flame are also depicted in Fig. 7. Along a radius, velocity is constant in the central unburned region of the fuel/air jet and decreases with a steep slope toward the outer stagnant condition. The scatter in the measured velocity at the 20 mm height exists because of the honeycomb flow straightener present in the fuel tube; the flow velocity near the burner surface depends on whether the measuring volume is above the wall of a honeycomb cell or above the opening of the cell. This effect diminishes downstream as the individual cell jets diffuse into a uniform flow. Peak velocities are between 3 m/s and
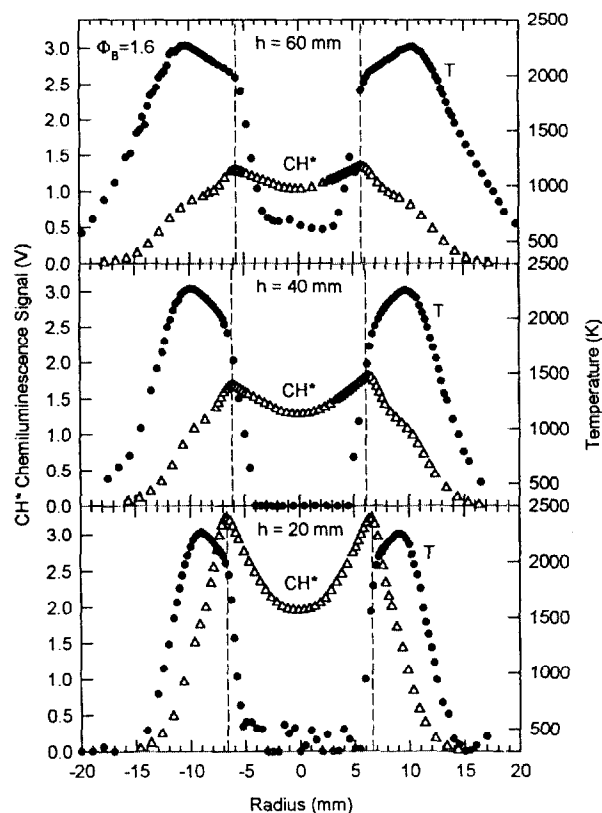
Fig. 8. Temperature and CH* chemiluminescence signal at 20 mm, 40 mm, and 60 mm above the burner in the $\Phi_B = 1.6$ flame.

3.5 m/s at each axial location. In this flame, the peak temperature of the outer nonpremixed flame occurs at the same location as the change in velocity gradient. This approximate coincidence of the location of the peak temperature and that of the change in velocity gradient in the nonpremixed flame region occurs because of gas expansion and is in agreement with that measured and predicted for laminar, coflow, pure diffusion flames by Mitchell et al. [58]. Although not shown here, measured peak velocities in the $\Phi_B = 2.0$ and $\Phi_B = 3.5$ flame were about 3 m/s and 2 m/s, respectively. These measured velocities were used to compute the radiation corrections for the temperature measurements.

Figure 8 shows line-of-sight CH* chemiluminescence profiles for the $\Phi_B = 1.6$ flame at heights of 20 mm, 40 mm, and 60 mm. The temperature profiles are also depicted for reference. Dashed vertical lines mark the locations of the peak CH* signals. As a result of the broad acceptance angle of the optics and the spatially

integrated nature of the measurement, the CH* profiles are unrealistically wide. The CH* signals peak at radii of 6.6 mm, 6.1 mm, and 5.8 mm from the burner centerline, for heights of 20 mm, 40 mm, and 60 mm, respectively. The CH* signals peak near the inner characteristic temperature associated with the premixed flame. Each CH* profile shows only one peak on each side of the radial centerline. The 40 mm and 60 mm-height CH* profiles appear to have inflection points near the outer nonpremixed flame location, which may indicate that double CH peaks exist. However, the inflection points may be caused by the temperature dependence of the CH* signal, and hence this evidence of double CH peaks is inconclusive. Although not shown in this paper, CH* profiles measured in $\Phi_B = 2.0$ and 3.5 flames were broad and did not show inflections away from the peak-signal locations [46].

Laser-induced-fluorescence profiles of CH along the central chord are depicted for the $\Phi_B = 1.6$ flame in Fig. 9. Temperature profiles are again repeated for reference, and dotted vertical lines mark the locations of the peak CH LIF signals. The CH LIF profiles are narrow, with FWHMs of less than 1.0 mm (in agreement with the narrowness of CH profiles measured in atmospheric-pressure diffusion flames [59]). The CH LIF profiles peak at 7.1 ± 0.1 mm, 7.2 ± 0.1 mm, and 7.1 ± 0.1 mm for heights of 20 mm, 40 mm, and 60 mm above the burner, respectively. The point-measured CH LIF signals peak at larger radii than the line-of-sight CH* signals. This is expected, since the line-of-sight CH* signal peaks when it contains contributions from two mirror-image CH* peaks along a chord. In agreement with the CH* results, the peak CH LIF signals exist near the characteristic temperature associated with the rich, premixed flame, and they do not peak near the outer nonpremixed flame. This indicates that either (a) there are no secondary CH concentration peaks, or (b) the combinations of CH number densities and local quenching environments render secondary CH signals undetectable. The CH LIF measurements exhibit scatter in the low-temperature, unburned, central fuel/air jet which is attributed to measurement noise and not to CH signal.
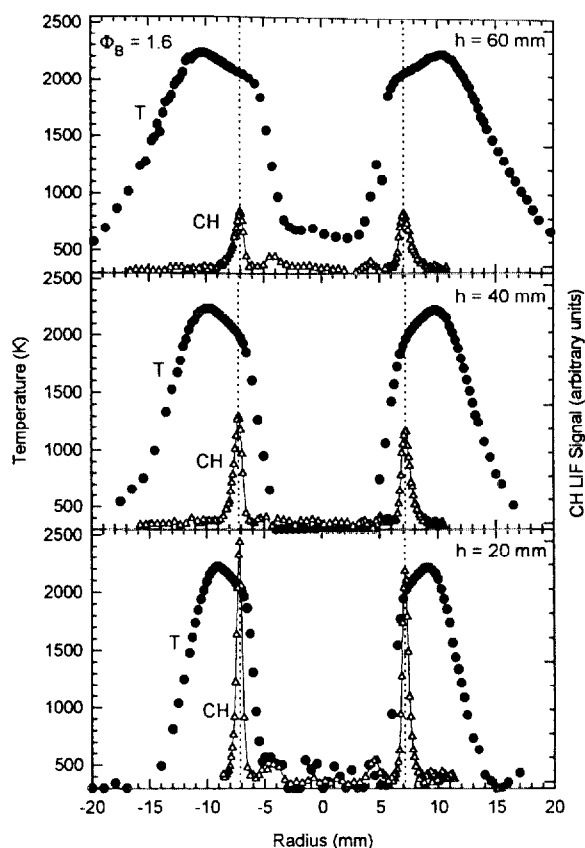
Figure 10 depicts radial TFP-determined

Fig. 9. Temperature and CH LIF signal at 20 mm, 40 mm, and 60 mm above the burner in the $\Phi_B = 1.6$ flame.



Fig. 10. Temperature and CH LIF signal at 20 mm, 40 mm, and 60 mm above the burner in the $\Phi_B = 2.0$ flame.

temperature profiles and LIF-determined CH profiles at three axial locations for the $\Phi_B = 2.0$ flame. Dotted vertical lines mark the locations of the CH LIF signal peaks. The temperature profiles for these flames exhibit the same basic trends as for the $\Phi_B = 1.6$ flame; however, the location of an inner characteristic temperature is not as easily distinguishable in these profiles, and the region of moderate slope (between the $CH_4$/air premixed component flame and the $CO/H_2$/air nonpremixed component flame) exhibits a larger gradient than that exhibited in the same region of the $\Phi_B = 1.6$ flame. Thus, the $\Phi_B = 2.0$ flame has a less defined double-flame structure, and more of a "merged"-flame structure (after Ref. 12). Peak temperatures are 2180 ± 82 K, 2200 ± 83 K, and 2130 ± 79 K at heights of 20 mm, 40 mm, and 60 mm above the burner. The CH LIF profiles peak at 8.1 ± 0.1 mm, 8.6 ± 0.1 mm, and 8.3 ± 0.1 mm for heights of 20 mm, 40 mm, and 60 mm above the burner, respectively. The CH LIF profiles
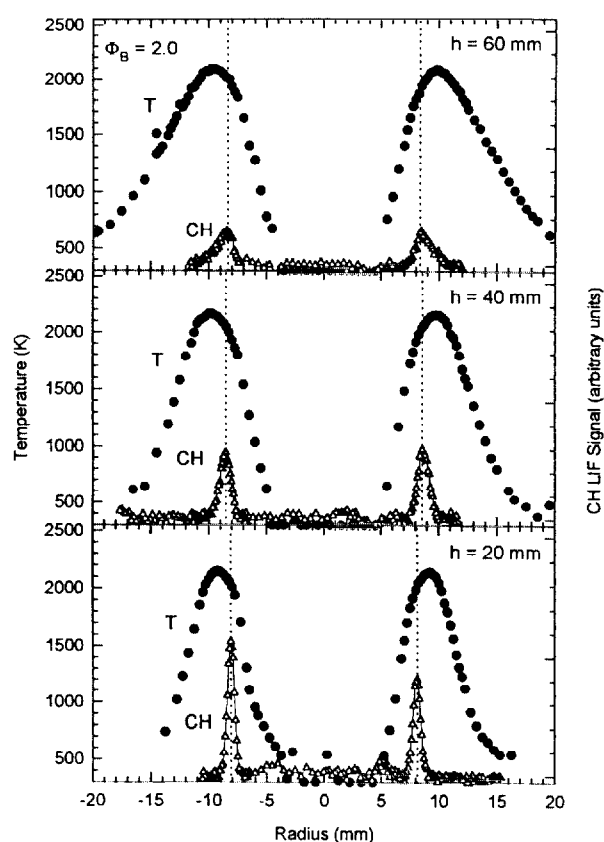
achieve maxima on the fuel side of the peak temperature.

Radial centerline temperature and CH LIF profiles for the $\Phi_B = 3.5$ flame at heights of 20 mm, 40 mm, and 60 mm are depicted in Fig. 11. Dotted vertical lines mark the locations of the CH LIF signal peaks. The inner characteristic temperature and the region of moderate slope are not apparent for the $\Phi_B = 3.5$ flame. Hence, this flame does not exhibit the double-flame structure. The shapes of the profiles are similar to those measured previously in laminar coflow methane–air jet diffusion flames [58]. Peak temperatures are 2130 ± 79 K, 2100 ± 77 K, and 1930 ± 67 K at heights of 20 mm, 40 mm, and 60 mm above the burner, respectively. The CH LIF profiles peak at 9.8 ± 0.1 mm, 9.5 ± 0.1 mm, and 9.1 ± 0.1 mm for heights of 20 mm, 40 mm, and 60 mm above the burner, respectively. The CH LIF profiles peak just on the fuel side of the temperature peaks, in agreement with previous measurements in pure diffusion flames [60]. Hence, based on temper-
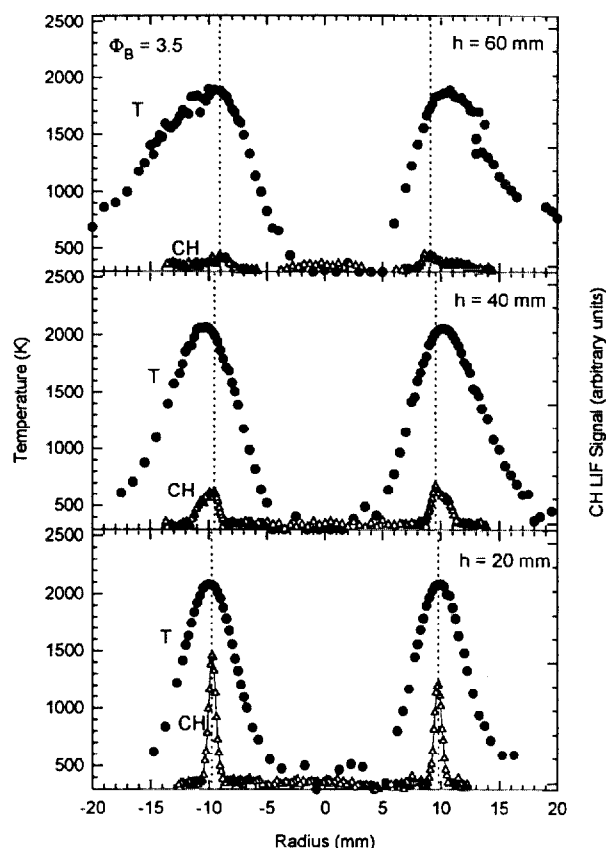
Fig. 11. Temperature and CH LIF signal at 20 mm, 40 mm, and 60 mm above the burner in the $\Phi_B$ = 3.5 flame.



Fig. 12. Locations of peak temperature, CH* chemiluminescence signal, and CH LIF signal for $\Phi_B$ = 1.6, 2.0, and 3.5 flames.

ature and CH location, the $\Phi_B$ = 3.5 flame behaves similarly to a pure diffusion flame. The temperature and CH results at heights of 40 mm and 60 mm above the burner are not smooth and/or narrow because of flame flicker.

The present study focused on three selected axial locations within each of three selected flames, chosen to match the measurement locations and operating conditions used in Ref. 16. Within the present detection limits, double CH radical peaks were not found on the same side of the radial centerline at heights of 20 mm, 40 mm, or 60 mm above the burner in the $\Phi_B$ =1.6, 2.0, or 3.5 flames. Hence, based on the present evidence, the existence of double CH peaks cannot be invoked to explain the $EINO_x$ minimum measured in these flames. It should be noted that the absence of secondary CH LIF *signal* peaks does not prove conclusively that double CH *concentration* peaks do not exist. Small CH peaks may not be detectable because of the effects of collisional quenching on the
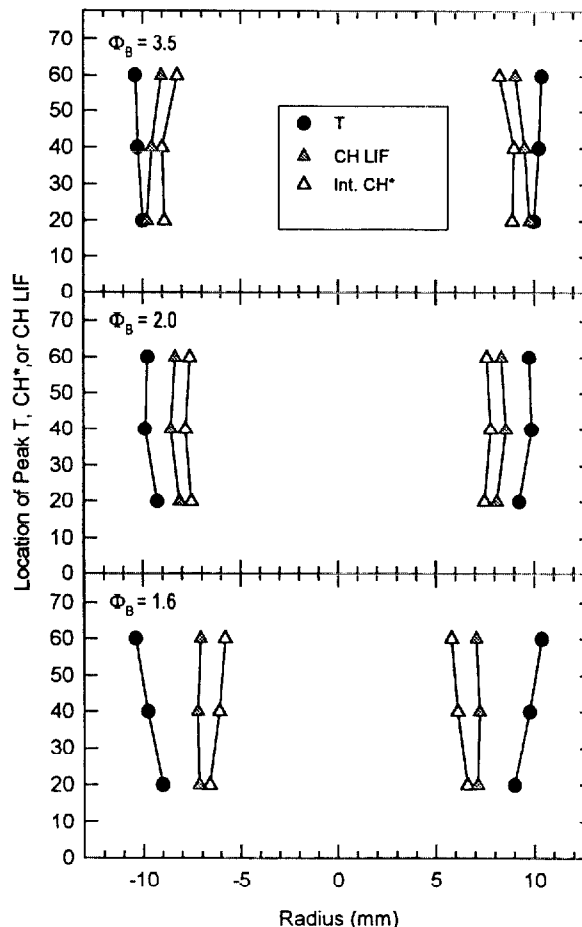
measurement, and this topic warrants further study.

Figure 12 depicts a summary of the locations of the maxima in the temperature, CH*, and CH LIF profiles for the $\Phi_B$ = 1.6, 2.0, and 3.5 flames. It is reemphasized that the CH* measurements are line-of-sight measurements, whereas the CH LIF and temperature measurements are point measurements taken along the central chord. For the $\Phi_B$ = 1.6 flame, the peak temperatures occur at increasing radii as axial distance increases, whereas the CH* and CH LIF peaks occur at decreasing radii. Hence, the radial locations corresponding to the peak temperature and CH signals move apart as distance above the burner increases. For the $\Phi_B$ = 2.0 flame, the radial locations of the peak temperature and CH signals increase together from 20 mm to 40 mm and then decrease together at

60 mm above the burner. The peak temperatures and CH signals are closer together in the $\Phi_B$ = 2.0 flame than in the $\Phi_B$ = 1.6 flame. For the $\Phi_B$ = 3.5 flame, the radial location of the peak temperature increases, while the radial locations of the maximum CH* and CH LIF signals decrease, with increasing distance above the burner. The peak temperatures and CH signals are even closer together in the $\Phi_B$ = 3.5 flame than in the $\Phi_B$ = 2.0 and $\Phi_B$= 1.6 flames. Hence, if the peak CH location marks the inner $CH_4$/air premixed flame and the peak temperature location marks the outer $CO/H_2$/air nonpremixed flame, the two flame fronts diverge in the near-burner region for the $\Phi_B$ = 1.6 flame, but they begin to merge together at lower levels of partial premixing ($\Phi_B$ = 2.0 and 3.5).

## SUMMARY AND CONCLUSIONS

Temperature and CH radical radial locations were measured at heights of 20 mm, 40 mm, and 60 mm above the burner in partially premixed $CH_4$/air flames with fuel-side equivalence ratios of 1.6, 2.0, and 3.5. The study was undertaken because an exhaust $EINO_x$ minimum was previously measured in these flames, and numerical modeling showed that locating CH radical is important for understanding the $EINO_x$ behavior. During this investigation, temperature, axial velocity, and CH radical location were added to an existing partially premixed flame database.

TFP was found to be more appropriate than thermocouple thermometry for measuring gas temperatures in partially premixed flames because TFP avoids the surface-ignition problems of a thermocouple in the rich unburned fuel/air mixture. A thermocouple-based calibration of TFP was successfully implemented in the present work, and radiation corrections were performed using actual measured velocities. The $\Phi_B$ = 1.6 operating condition exhibited double-flame temperature behavior, the $\Phi_B$ = 2.0 flame exhibited more of a merged-flame behavior, and the $\Phi_B$ = 3.5 flame exhibited behavior similar to a pure diffusion flame. In the $\Phi_B$ = 1.6 double flame and in the $\Phi_B$ = 2.0 merged flame, both the line-of-sight CH* chemiluminescent signal and the centerline point-by-point CH LIF signal exhibited maxima

at locations coincident with the temperature of the rich premixed hydrocarbon/air component flame. The existence of double CH peaks cannot presently be invoked to help explain the exhaust $EINO_x$ minimum. In the near-burner region, the premixed and nonpremixed component flames of the double flame separate with increasing downstream distance, while they merge together at lower levels of partial premixing.

## REFERENCES

1. Yamaoka, I., and Tsuji, H., *Seventeenth Symposium (International) on Combustion*, The Combustion Institute, Pittsburgh, 1979, p. 843.
2. Yamaoka, I., and Tsuji, H., *Sixteenth Symposium (International) on Combustion*, The Combustion Institute, Pittsburgh, 1977, p. 1145.
3. Yamaoka, I., and Tsuji, H., *Fifteenth Symposium (International) on Combustion*, The Combustion Institute, Pittsburgh, 1975, p. 637.
4. Seshadri, K., Puri, I., and Peters, N., *Combust. Flame* 61:237 (1985).
5. Hamins, A., Thridandam, H., and Seshadri, K., *Chem. Eng. Sci.* 40:2027 (1985).
6. Smooke, M. D., Seshadri, K., and Puri, I. K., *Twenty-Second Symposium (International) on Combustion*, The Combustion Institute, Pittsburgh, 1988, p. 1555.
7. Law, C. K., Zhu, D. L., Li, T. X., Chung, S. H., and Kim, J. S., *Combust. Sci. Technol.* 64:199 (1989).
8. Li, S. C., Ilincic, N., and Williams, F. A., *J. Eng. Gas Turbines Power* 119:836 (1996).
9. Dupont, V., and Williams, A., *Combust. Flame* 114:103 (1998).
10. Dupont, V., Pourkashanian, M., Richardson, A. P., Williams, A., and Scott, M. J., *Transport Phenomena in Combustion, Volume 1*, Taylor and Francis, 1996, pp. 263–274.
11. Nishioka, M., Nakagawa, S., Ishikawa, Y., and Takeno, T., *Combust. Flame* 98:127 (1994).
12. Tanoff, M. A., Smooke, M. D., Osborne, R. J., Brown, T. M., and Pitz, R. W., *Twenty-Sixth Symposium (In-*

ternational) on Combustion, The Combustion Institute, Pittsburgh, 1996, p. 1121.

13. Tseng, L.-K, Gore, J. P., Puri, I. K., and Takeno, T., Twenty-Sixth Symposium (International) on Combustion, The Combustion Institute, Pittsburgh, 1996, p. 993.

14. Greenberg, J. B., and Sarig, N., Combust. Flame 104:431 (1996).

15. Blevins, L. G., and Gore, J. P., Combust. Flame 116:546 (1999).

16. Gore, J. P., and Zhan, N. J., Combust. Flame 105:414 (1996).

17. Van Oostendorp, D. L., Borghols, W. T. A., and Levinsky, H. B., Combust. Sci. Technol. 79:195 (1991).

18. Kim, T. K., Alder, B. J., Laurendeau, N. M., and Gore, J. P., Combust. Sci. Technol., 110:361 (1996).

19. Nguyen, Q. V., Dibble, R. W., Carter, C. D., Fiechtner, G. J., and Barlow, R. S., Combust. Flame 105:499 (1996).

20. Lee, B. J., Cha, M. S., and Chung, S. H., Combust. Sci. Technol. 127:55 (1997).

21. Chou, C. P., Chen, J. Y., Yam, C. G., and Marx, K. D., Combust. Flame 114:420 (1998).

22. Shu, Z., Aggarwal, S. K., Katta, V. R., and Puri, I. K., Combust. Flame 111:276 (1997).

23. Shu, Z., Aggarwal, S. K., Katta, V. R., and Puri, I. K., Combust. Flame 111:296 (1997).

24. Rogg, B., Behrendt, F., and Warnatz, J., Twenty-First Symposium (International) on Combustion, The Combustion Institute, Pittsburgh, 1986, p. 1533.

25. Roper, F. G., Einarsson, S., and Kayes, P. J., Fuel 57:187 (1978).

26. Driscoll, J. F., Chen, R. H., and Yoon, Y., Combust. Flame 88:37 (1993).

27. Rokke, N. A., Hustad, J. E., and Otto, K. S., Combust. Flame 97:88 (1994).

28. Muler, C. M., Breitbach, H., and Peters, N., Twenty-Fifth Symposium (International) on Combustion, The Combustion Institute, Pittsburgh, 1994, p. 1099.

29. Turns, S. R., Myhr, F. H., Bandaru, R. V., and Maund, E. R., Combust. Flame 93:255 (1993).

30. Lee, T.-W., Fenton, M., and Shankland, R., Combust. Flame 109:536 (1997).

31. Lee, B. J., Cha, M. S., and Chung, S. H., Combust. Sci. Technol. 127:55 (1997).

32. Lyle, K. H. (1997). M. S. thesis, Purdue University.

33. Lyle, K. H., Tseng, L. K., Gore, J. P., and Laurendeau, N. M., Combust. Flame 116:627 (1999).

34. Blevins, L. G., and Gore, J. P., Combust. Sci. Technol. 109:255 (1995).

35. Gollahalli, S. R., and Subba, S., J. Propul. Power 13:226 (1997).

36. Chakka, R. K. (1996). M.S. thesis, Purdue University.

37. Zhan, J. (1994). M.S. thesis, Purdue University.

38. Vilimpoc, V., Goss, L. P., and Sarka, B., Opt. Lett. 13:93 (1988).

39. Goss, L. P., Vilimpoc, V., Sarka, B., and Lynn, W. F., J. Eng. Gas Turbines Power 111:46 (1989).

40. Vilimpoc, V., and Goss, L. P., Twenty-Second Symposium (International) on Combustion, The Combustion Institute, Pittsburgh, 1988, p. 1907.

41. Chen, T. H., and Goss, L. P., J. Propulsion and Power 8:16 (1992).

42. Chen, T. H., Goss, L. P., Talley, D. G., and Mikolaitis, D. W., J. Propul. Power 8:548 (1992).

43. Roberts, W. L., Driscoll, J. F., Drake, M. C., and Goss, L. P., Combust. Flame 94:58 (1993).

44. Bedat, B., Giovannini, A., and Pauzin, S., Exp. Fluids 17:397 (1994).

45. Pitts, W. M., Twenty-Sixth Symposium (International) on Combustion, The Combustion Institute, Pittsburgh, 1996, p. 1171.

46. Blevins, L. G. (1996). Ph.D. thesis, Purdue University.

47. Incropera, F. P., and DeWitt, D. P., Fundamentals of Heat and Mass Transfer, 3rd ed., John Wiley & Sons, New York, 1990, p. 711.

48. Moore, J. H., Davis, C. C., and Coplan, M. A., Building Scientific Apparatus: A Practical Guide to Design and Construction, Addison-Wesley, New York, 1989, p. 184.

49. American National Standard for Expressing Uncertainty—U.S. Guide to the Expression of Uncertainty in Measurements, ANSI/NCSL Z540-2-1997, American National Standards Institute, National Conference of Standards Laboratories, Boulder, Colorado, 1997.

50. Taylor, B. N., and Kuyatt, C. E. (1994). Guidelines for Evaluating and Expressing the Uncertainty of NIST Measurement Results, National Institute of Standards and Technology Technical Note 1297.

51. Morgan, V. T., Advances in Heat Transfer, Vol. 11, Academic Press, New York, 1975, p. 199.

52. Hsu, S. T., Engineering Heat Transfer, D. Van Nostrand, Princeton, NJ, 1963.

53. Kelkar, A. S. (1996). M.S. thesis, Purdue University.

54. Kohse-Hoinghaus, K., Prog. Energy Combust. Sci. 20: 203 (1994).

55. Daily, J. W., Prog. Energy Combust. Sci. 23:133 (1997).

56. Renfro, M. W., Klassen M. S., King, G. B., and Laurendeau, N. M., Opt. Lett. 22:175 (1997).

57. Renfro, M. W. (1997). M.S. thesis, Purdue University.

58. Mitchell, R. E., Sarofim, A. F., and Clomburg, L. A., Combust. Flame 37:227 (1980).

59. Norton, T. S., and Smyth, K. C., Combust. Sci. Technol. 76:1 (1991).

60. Norton, T. S., Smyth, K. C., Miller, J. H., and Smooke, M. D., Combust. Sci. Technol. 90:1 (1993).